PhD Thesis

Experimental studies on dispersion processes in periodic flows

By

Annalisa De Leo

UNIVERSITÀ DEGLI STUDI
DI GENOVA

Department of Civil, Chemical and Environmental Engineering

Advisors

Prof. Alessandro Stocchino

Prof. Nicoletta Tambroni

April 2022

Annalisa De Leo

PhD in Civil, Chemical and Environmental Engineering

Curriculum of Fluid Dynamics and Environmental Engineering, XXXIV cycle

Dipartimento di Ingegneria Civile, Chimica e Ambientale

Universitá degli Studi di Genova, Italy

email: annalisa.deleo@edu.unige.it

PhD supervisors:

Prof. Alessandro Stocchino - Hong Kong Polytechnic University, Hong Kong, China

Prof. Nicoletta Tambroni - Universitá degli Studi di Genova, Italy

Reviewers:

Prof. Andrea Defina - Dipartimento di Ingegneria Civile Edile e Ambientale, UNIPD, Universitá degli Studi di Padova, Italy

Prof. Arnoldo Valle-Levinson - Department of Civil and Coastal Engineering, University of Florida, USA

Exam committee:

Prof. Michele Bolla Pittaluga - Dipartimento di Ingegneria Civile, Chimica e Ambientale, Universitá degli Studi di Genova, Italy

Prof. Costantino Manes - Dipartimento di Ingegneria Ambientale, del Territorio e delle Infrastrutture, Politecnico di Torino, Italy

Prof. Rosaria Ester Musumeci - Dipartimento di Ingegneria Civile e Architettura, Universitá degli Studi di Catania, Italy

Prof. Luca Solari - Dipartimento di Ingegneria Civile e Ambientale, Universitá degli Studi di Firenze, Italy

Prof, Rodolfo Repetto - Dipartimento di Ingegneria Civile, Chimica e Ambientale, Universitá degli Studi di Genova, Italy

Date of the Defense: April 14, 2022

In memory of my beloved grandma Anna ♡

SUMMARY

The aim of this thesis *Experimental studies on dispersion processes in periodic flows* is to study the hydrodynamics and asses the mixing properties of periodic flows, through extensive experimental campaigns. With *mixing*, we refer to the field of environmental fluid mechanic that seeks to provide tools to assess the flow of nutrients needed for the survival of an ecosystem, limit toxic pollutants and minimize the anthropic impact. Over the last twenty years, a lot of literature had been devoted to asses mixing processes occurring in uniform flows but less on periodic ones. A periodic flow is an oscillatory flow whose characteristics assume the same sequence of values exactly after a fixed length of time, known as the period. These repetitive velocity patterns produce in the hydrodynamics a periodical occurrence and, eventually, destruction of flow structures responsible for the dispersion or the entrainment of pollutants/ nutrients within the domain considered. Coastal areas provide a typical example of regions dominated by period flows, such as those induced by tidal currents and sea waves. These areas are also characterised by a massive human development, and biodiverse ecosystems, making the study of the mixing of paramount importance for their sustainment and preservation. The thesis is composed by two main Parts, each one dealing with a different experimental campaign.

In particular, the purpose of Part I is to study the processes that govern the dynamics of periodic non-uniform flows by conducting experiments on a physical model that represents a tidal environment with a barrier island inlet and a tidal channel surrounded by flats. Starting from the study of a single component tide, we refine our results studying more complicated tidal shapes, consisting of multi harmonics laws. In both cases, the results show that small pair separations grow exponentially in time whereas larger separations are controlled by large scale structures. Lagrangian Coherent Structures (LCS) have been detected, suggesting that material curves exist and map transport boundaries within the domain. Moreover, in order to understand how energy is exchanged among the wide range of flows, we analyze nonlinear energy/enstrophy transfer rates and map out the energy pathways through the flow scales of the measured velocity fields.

Part II approaches both experimentally and numerically the study of plastic particle transport owed to the action of sea waves. The experiments are performed in a wave flume, forced by regular waves. The main objective is to quantify the inertial effect of the heavy particles on the Stokes drift and, ultimately, to suggest a new analytical formulation for the net settling velocity, through the comparison between experimental results and those provided by a simplified numerical model. Experiments suggest that the inertial effects lead to an increased particle settling velocity with respect to the one predicted by standard formulas validated in still fluids. Numerical simulations lead to the conclusion that sea waves are able to generate a net Lagrangian transport by the Stokes drift, which is considered an important source of mass transport in coastal areas.

TABLE OF CONTENTS

LIST OF TABLES

TABLE **Page**

List of Figures

Figure **Page**

Part I

Dispersion processes in weakly dissipative tidal channels

"All models are wrong, but some are useful."

– George E.P. Box

List of Symbols

K	absolute diffusivity
$\boldsymbol{A}^2$	absolute dispersion tensor
h_b	basin depth
w_b	basin width
$\boldsymbol{C}$	Cauchy- Green tensor
C	Chézy coefficient
w_{ch}	channel width
L_0	characteristic length
R^2	Coefficient of determination: R-squared
L_b	convergence length
γ	convergence parameter
r_h	depth ratio parameter
ϵ	dimensionless tidal amplitude, if not stated otherwise
λ_1 , λ_2	eigenvalues
e_1 , e_2	eigenvectors
T_n	exit time
Γ	Finite Size Lyapunov Exponent
$\sigma_{t_0}^{t_1}$	Finite Time Lyapunov Exponent
$\boldsymbol{\Phi}$	flow map
$\mathscr{B}$	fluid body
F	form factor
η	free surface elevation

H	free surface level
χ	friction parameter
j	friction term
F_r	Froude number
δ	FSLE multiplier
α, β	generic exponents, if not stated otherwise
h_w	inlet water depth
w_i	inlet width
L_g	inviscid length
$\boldsymbol{J}$	Jacobian matrix
E_k	kinetic energy
$\mathscr{R}$	Lagrangian autocorrelation function
$\boldsymbol{\xi}$	Lagrangian coordinate system
T_L	Lagrangian integral scale
E_L	Lagrangian kinetic energy
D_0	mean water depth
Π	non linear energy flux
Z	non linear enstrophy flux
S_n	normal strain tensor
λ_0	Okubo-Weiss parameter
P	power per unit mass
D	relative diffusivity
$\boldsymbol{R}^2$	relative dispersion tensor
Re	Reynold's number
r	separation length
S_s	shear strain tensor
S	strain tensor
S_t	Strouhal number
λ_{ci}	swirling strength

a_d	tidal amplitude (diurnal)
a	tidal amplitude (general)
a_{sd}	tidal amplitude (semi-diurnal)
ω_d	tidal angular frequency (diurnal)
ω	tidal angular frequency (general)
ω_{sd}	tidal angular frequency (semi-diurnal)
T_d	tidal period (diurnal)
T	tidal period (general)
T_{sd}	tidal period (semi-diurnal)
ϕ	tidal phase shift
a^2	total absolute dispersion
Z^2	total enstrophy
r^2	total relative dispersion
T_T	turn over time
W^u	unstable manifold
$\nabla \boldsymbol{v}$	velocity gradient tensor
l_i	vertical plate length
ω_z	vorticity
k	wavelength

CHAPTER 1

INTRODUCTION

Estuaries are considered transitional regions between landward waters and open sea, and thus important sites for human development. Estuarine regions can be classified depending on morphology, geometry configurations, vertical salinity stratification and finally hydrodynamics (MacCready and Geyer, 2010; Valle-Levinson, 2010). In particular, coastal bays and estuaries are characterized by flows driven by hydraulic imbalance such as baroclinic pressure gradients, river inflows, wind stresses, and tidal waves. In a recent contribution (Valle-Levinson, 2021), a classification based on the dynamical balance between different mechanical drivers (tides and density gradients) has been suggested in particular for semienclosed basins.

If on one hand, tidal propagation has been deeply studied in order to better understand the suitable parameters to describe it (Seminara et al., 2010; Toffolon et al., 2006; Cai et al., 2012), on the other hand, the role of tides on mass transport still requires a thorough investigation. The role of tidal circulation in estuarine mixing was considered of less importance for several decades (Geyer and MacCready, 2014). However, the so-called residual currents derived by averaging flow field over a tidal period are recognized to be fundamental agents for mass transport and dispersion processes (Jay, 1991; Zimmerman, 1986) owing to the strong and persistent straining and shearing (Ridderinkhof and Zimmerman, 1992).

Some geometrical features such as tidal embankments or coastal lagoons, combined with the

periodic nature of the tidal forcing, may trigger the generation of flow structures that enhance the dispersion mechanisms. These flow structures arose are characterize by different length scales. The presence of a tidal inlet, for example, can generate macro-vortices that during a tidal cycles may influence the momentum and mass transport on relatively large distances, about four time the tidal inlet width (Awaji et al., 1980; Awaji, 1982; Branyon et al., 2021).

Several studies focused on the definition of the time scales and the estimation of the dispersion coefficients in monochromatic tidal force conditions (see Cucco et al. (2009); Umgiesser et al. (2014); Viero and Defina (2016) among others). At the same time, several works were dedicated to the prediction of multi-harmonic tides (Amin, 1986; Lee and Chang, 2019) and their propagation (Jay, 1991; Seminara et al., 2010; Fortunato and Oliveira, 2005; Toffolon et al., 2006; Cai et al., 2012). However, literature on the effects of multiple harmonics on the flow field and dispersion processes is lacking. In fact, field studies devoted to estimation of longitudinal dispersion coefficients (Monismith et al., 2002; Lewis and Uncles, 2003; Banas et al., 2004) did not provide any relationship among the coefficients and the tidal wave shapes, such as tidal asymmetries or seasonal modulations. Several field measurements of longitudinal dispersion coefficient reported a wide range of values, spanning almost two order of magnitudes from 10 to 10^3 m^2/s^{-1} (Fischer et al., 1979; Monismith et al., 2002; Lewis and Uncles, 2003; Banas et al., 2004). Moreover, tides tend to produce non-monotonic particle velocity correlation leading to possible particle looping trajectories that also reflect on a looping character of the Lagrangian integral time scales, differently from the classical statistically steady or homogeneous turbulence (Orre et al., 2006; Enrile et al., 2019). Looping-like particle trajectories have been also studied in oceanic context and they were found to be related to anomalous dispersion regimes (Berloff et al., 2002; Veneziani et al., 2004; Enrile et al., 2019).

Seeking a reliable definition of the time scale for transport processes led to use different measures such as residence time, flushing time, age (see Cucco et al. (2009); Umgiesser et al. (2014); Viero and Defina (2016); Yang et al. (2018) among many others). The attempt was to classify estuaries based on these time scales and an example can be found in Umgiesser et al. (2014) where several estuaries and coastal bays of the Mediterranean Sea were compared. However, most of these time scales were based on Eulerian concepts and quite a few on Lagrangian

approaches.

Classical analyses in terms of single and multiple particle statistics are very seldom applied to estuaries compared to oceanographic and atmospheric applications (LaCasce, 2008). Moreover, attempts to study the dispersion processes under controlled laboratory conditions in simplified estuaries are very limited in literature (Kusumoto, 2008; Nicolau del Roure et al., 2009; Dronkers, 2019), although worth pursuing. Indeed, controlled experiments with simple boundary conditions provide a measure of some of the main mechanisms that drive the dispersion process. The definition of these mechanism is a goal quite difficult to achieve on the basis of field observations whose interpretation is generally complicated by the large scale of the processes, more irregular natural geometries and the simultaneous presence of a variety of features whose role cannot be readily isolated. Moreover, they provide an useful data-set to test reliability of analytical and numerical models.

In the present study, we aim to investigate the relevant dispersion processes using a large scale physical model of a weakly-dissipative tide dominated estuary (Toffolon et al., 2006; Cai et al., 2012) characterized by the presence of an inlet mouth that connects the outer sea to a compound tidal channel. Flow is forced by tidal waves imposed at the outer basin.
In an attempt to understand the role of the tidal constituents, we designed this study with the aim to firstly investigate the role of a single harmonic and secondly the role of two harmonics, representing the semi-diurnal and diurnal components, with different tidal form factor. We provide a detailed description of the transient macro-vortices generated at the inlet and the resulting residual current for the different tidal forcings. The generation of flood-vortices is compared with previous works (Nicolau del Roure et al., 2009) and extended considering the effect of the vorticity generation owing to the depth jump between the channel and the tidal flats (Brocchini and Colombini, 2004; Stocchino et al., 2011).
Large scale Particle Image Velocimetry is employed to measure two dimensional (x-y) surface velocity fields providing a high spatial and temporal description of the flow. A detailed Lagrangian analysis of the typical integral scales and of single and multiple particle statistics is performed and provides a clearer picture of the processes occurring in weakly dissipative estuaries that depend on the controlling parameter such as the amplitude or the period of the forcing tide.

The flow structures at different scales generated by the interaction of the tidal waves with the inlet mouth are expected to be further complicated by increasing the complexity of the tidal waves, with possible effects on the main dispersion processes. To assess the interplay of the flow structures at different scales and the resulting dispersion regimes, multiple particle statistics have proven to be an effective analysis when applied to geophysical flows (Orre et al., 2006; LaCasce, 2008). Moreover, the theoretical results in terms of relative dispersion and Finite Size Lyapunov Exponents suggest the possible existence of local and non-local dynamical behaviours (Kraichnan, 1966; Lin, 1972; Bennett, 1984; Babiano et al., 1990). In particular, the non-local regimes are associated to particle separations that are influenced by different flow scales. Applications to geophysical flows showed the existence of local and non-local regimes when the flow is mainly generated by the tides (Enrile et al., 2019). In the present study, we will perform multiple particles statistics based on the measured flow fields generated by both a single harmonic and multiple harmonics tides.

Moreover, geophysical flows act as vectors of pollutants and nutrients, posing a challenge when attempting to describe the dispersion processes. What at first sight may appear chaotic and indescribable, in-depth analysis reveals special surfaces of fluid trajectories that act as dynamical attractors.

The Lagrangian Coherent Structure theory, first introduced by G.Haller, seeks to reveal the skeleton of the turbulence (Mathur et al., 2007; Haller, 2011; Haller and Beron-Vera, 2012; Haller, 2015). As underlined by Haller (2015), classical dynamical systems theory gives insights on Lagrangian Coherence in time independent, time periodic and quasi-periodic velocity fields.

Already with the simplified geometry and forcing used for the present experiments, the resulting flow fields show complex dynamical processes at different scales. Single and multiple particle statistics implicitly assume homogeneity of the flow.

To fully understand the role of the non homogeneous character of the flow, we apply Haller's theory for the computation of the Finite Time Lyapunov Exponents fields seeking for the identification of possible LCSs. The final part of Part 1 is dedicated to the study of the non-linear energy and enstrophy transfers. It is well known the relation between the multiple statistics regimes and the energy cascade. However, we aim to go beyond a simple spectral analysis, studying in

details the energy/enstrophy transfers among the different scales.

Part 1 of the present thesis is organized as follows. Chapter 2 presents the experimental set-up, the experiments run and the measuring technique. Chapter 3 is devoted to a general background theory. Chapter 4 deals with the analysis of a dataset of surface velocity fields and the results of the Lagrangian analysis performed. Chapter 5 focuses on the energy flux transport among the scales involved in the process, introducing also the theory underneath. Chapter 6 concludes this first part of the thesis.

CHAPTER 2

EXPERIMENTAL SET-UP AND MEASURING TECHNIQUE

2.1 PHYSICAL MODEL AND TIDAL FORCING

Physical experiments have been carried out in the hydraulic Laboratory of the Department of Civil, Chemical and Environmental Engineering (DICCA) of the University of Genova, Italy. A sketch of the overall experimental set-up is shown in Figure 2.1. The experimental apparatus can be divided in two main parts: a tidal channel and a rectangular basin, connected each other through a tidal inlet. In particular, the 23 m long tidal channel is characterized by a symmetrical compound cross-section, i.e. composed by a deep main channel and two lateral flats. Overall the tidal channel system is 2.42 m wide (w_{ch}), but the main channel has a landward decreasing width, starting from about 70 cm at the tidal inlet (w_i) reaching about 11 cm at the channel end. Consequently, the two tidal flats have a varying width between 0.86 m and 1.16 m on each side. This convergence feature is common in real tidal channels that are typically characterized by a landward convergence (Friedrichs and Aubrey, 1994) and a meandering behavior (this latter aspect not represented in our experimental apparatus for the sake of simplicity). The main channel has a longitudinal slope equal to 2.5‰ and tidal flats are located at a constant elevation of 0.24 m from the bottom of the channel. The basin, representing the sea, is 6 m long and 2.20 m wide (w_b), allowing for a maximum depth equal to h_b = 0.5

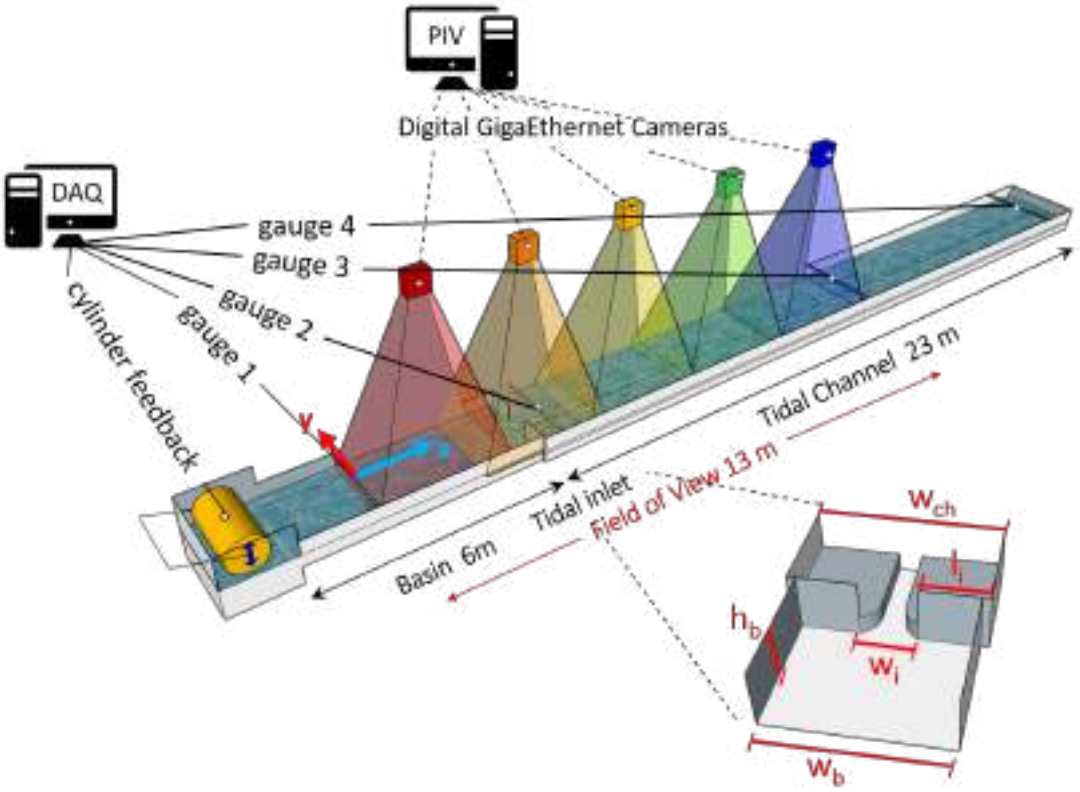

Figure 2.1: Sketch of the experimental set up and measuring systems.

m. Contrary to the tidal channel, the bottom of the basin is flat. The mean water elevation, referred to the bottom of the channel, at the channel inlet has been maintained constant and equal to h_w = 0.36 m during the experimental campaign. As already mentioned, the connection between the two main parts is made through a tidal inlet. It consists of two thin vertical plates l_i= 0.84 m placed at the seaward tidal flats edges, hence water exchange between the basin and the channel is allowed only at the inlet cross section of the main tidal channel. This is a common configuration in estuaries characterized by the so called *barrier island*, accumulations of sediments partially emerged between two inlets, constituted as a result of subsequent marine depositions and erosional processes occurring in the shoreline region. The inlet opening has not been altered during the whole experimental campaign.

The entire experimental apparatus is made by concrete providing an estimated conductance coefficient C of about 12 $m^{1/2}/s$, which corresponds to a Manning's resistance coefficient of about

Figure 2.2: Left panel) The oscillating cylinder and feeding tank. Right panel) The sloping mound at the opposite end.

$0.0167\ \mathrm{sm}^{-1/3}$.

In order to provide an oscillating water level, a tidal generator system has been installed at the end of the rectangular basin, in an adjacent feeding tank. It consists of a cylinder, with length of 2.8 m and diameter of 1,1 m (Figure 2.2), that imposes volume waves with variable period and amplitude. It is important to note that, in order to reduce wave reflections, a dissipative sloping mound has been installed at the end of the tidal channel (at the opposite side of the oscillating cylinder, see Figure 2.2). Moreover, in order to avoid the generation of surface waves, two free floating polystyrene sheets have been placed just in front of the oscillating cylinder: these damped water surface oscillations of high frequency generated by localized disturbances.

The cylinder is remotely controlled using a digital signal acquisition/ generation system and it provides a time law signal that, in its most general formulation, reads:

$$\eta(t) = \sum_i a_i \sin(\omega_i t + \phi_i) \tag{2.1}$$

where t is the time, η the free surface elevation, a_i the tidal amplitude, ϕ_i is the phase shift and $\omega_i = 2\pi/T_i$ the tidal angular frequency, being T_i the tidal period. Note that the subscript i stands for the i^{th} tidal component. In the following, we take advantage of this general formulation in distinguish between *single* component tides and *multiple* components tides. A list of the *single* and *multiple* component experiments can be found in Table 2.1, reporting the main parameter for each run.

Table 2.1: Experimental forcing tide parameters

	exp.	a [m]	D_0 [m]	T [s]
single component series	08-SC	0.0010	0.12	160
	09-SC	0.0037	0.12	160
	10-SC	0.0055	0.12	160
	11-SC	0.0081	0.12	160
	12-SC	0.0093	0.12	160
	13-SC	0.0013	0.12	100
	14-SC	0.0026	0.12	100
	15-SC	0.0044	0.12	100
	16-SC	0.0076	0.12	100
	17-SC	0.0118	0.12	100
	18-SC	0.0013	0.12	130
	19-SC	0.0027	0.12	130
	20-SC	0.0044	0.12	130
	21-SC	0.0062	0.12	130
	22-SC	0.0079	0.12	130
	23-SC	0.002	0.12	180
	24-SC	0.0039	0.12	180
	25-SC	0.0055	0.12	180
	26-SC	0.0076	0.12	180
	27-SC	0.0091	0.12	180

		exp.	a_{sd} [m]	a_d [m]	$T_{sd}[s]$	ϕ	F
multi components series	series 1	01-MC	0.017	0.0015	100	0	0.08
		02-MC	0.013	0.003	100	0	0.2
		03-MC	0.013	0.0035	100	0	0.3
		04-MC	0.012	0.0046	100	0	0.4
		05-MC	0.0075	0.006	100	0	0.8
		06-MC	0.006	0.007	100	0	1.2
		07-MC	0.005	0.008	100	0	1.6
	series 2	08-MC	0.013	0.003	100	$-\phi/4$	0.2
		09-MC	0.013	0.0035	100	$-\phi/4$	0.3
		10-MC	0.012	0.0046	100	$-\phi/4$	0.4
		11-MC	0.0075	0.006	100	$-\phi/4$	0.8
		12-MC	0.006	0.007	100	$-\phi/4$	1.2
		13-MC	0.005	0.008	100	$-\phi/4$	1.6
	series 3	14-MC	0.013	0.003	100	$\phi/4$	0.2
		15-MC	0.013	0.0035	100	$\phi/4$	0.3
		16-MC	0.012	0.0046	100	$\phi/4$	0.4
		17-MC	0.0075	0.006	100	$\phi/4$	0.8
		18-MC	0.006	0.007	100	$\phi/4$	1.2
		19-MC	0.005	0.008	100	$\phi/4$	1.6

With the aim to simplify our first approach to the tidal mixing problem, we decided to focus on the simplified single harmonic tide. It is characterized by a unique period and amplitude, reducing the general formulation of equation (2.1) to

$$\eta(t) = a \sin(\omega t). \tag{2.2}$$

In particular, in our first set of experiment we considered 5 different amplitudes a for 4 tidal periods $T = 2\pi/\omega$, for a total amount of 20 experiments.
However, astronomical tide is indeed provided by a wide variety of harmonic constituents each one associated to a different gravitational force interaction among Earth, Moon and Sun. In terms of amplitude, the first four main tidal contributions are: the principal lunar semi-diurnal (M2, 12.42 h period), the principal lunar diurnal (O1, 25.82 h), the principal solar semi-diurnal (S2, 12 h), and the principal solar diurnal (K1, 23.93 h) . Grouping together the diurnal and semi-diurnal components, a simplified form for the astronomical tidal free surface oscillation reads:

$$\eta(t) = a_{sd} \sin(\omega_{sd} t) + a_d \sin(\frac{\omega_{sd}}{2} t + \phi) \tag{2.3}$$

where we consider the period of the semi-diurnal component ($\omega_{sd} = 2\pi/T_{sd}$) as the reference one, i.e. the diurnal component period is simply twice the semi-diurnal component one. The relative importance of the semi-diurnal and diurnal components can be expressed through the form factor F defined as Lee and Chang (2019):

$$F = \frac{a_d}{a_{sd}} \tag{2.4}$$

The form parameter can be used to discriminate the different types of astronomical tide, in particular:

- if $F < 0.25$, the tide is semi-diurnal;
- if $0.25 < F < 1.25$, the tide is mixed, but mainly semi-diurnal;
- if $1.25 < F < 3.0$, the tide is mixed, but mainly diurnal;
- if $F > 3.0$, the tide is diurnal.

According to Tsimplis et al. (1995), the form parameter associated with the astronomical tide observed in different places in the Mediterranean Sea spans over a wide range of values. In our experiments we have thus considered different tidal forcing with form parameter varying between 0.038 and 1.7. We acknowledge that observed semi-diurnal (M_2, S_2) and diurnal (K_1, O_1) are characterized by different periods and this difference in periods leads to modulations with variations on longer periods (spring tide - neap tide cycles). However, reproducing these modulations at laboratory scales would require the acquisition of an unmanageable number of images, since our statistics are based on the average of several periods based on the slowest modulation, i.e. over the largest period. However, we introduced the phase shift in equation (2.1) to understand the role of the tidal wave shape depending of the phase lag between the semi-diurnal and diurnal constituents. Three series of experiments have been performed for a total of 19 experiments varying the form factor F and the phase ϕ, see Table 2.1 for the relevant experimental parameters. In particular, a first series of experiments (experiments from 1 to 7) has been designed for different values of the form factor and vanishing phase. A second series (from experiment 8 to 13) has been performed for the same form factor of the first series, but choosing $\phi = -\pi/4$. The phase shift has been changed to $\phi = \pi/4$ in the final series (from experiment 14 to 19).

2.2 MEASURING TECHNIQUE

2.2.1 LEVEL MEASUREMENT

During each experiment, water level and surface velocities have been measured.
In particular, free surface elevation was monitored using four ultrasound gauges (Honeywell model 946-A4V-2D-2C0-380E, with 30 cm range and an accuracy of 0.2% of the full scale), fixed on four aluminum profiles that allowed to place the gauges on the axis of the channel respectively at a distance of 3, 7.75, 17.3 and 28 m from the wave maker, see Figure 2.1 for position and Figure 2.3 for gauge detail. The gauge outputs are voltage measurements as function of time. The voltage readings are then transformed in metric measurements through a calibration curve. All ultrasound gauges have been calibrated and a linear law have been found with an R^2 close to

Figure 2.3: Ultrasound Gauge detail.

one as reported below (refers to Figure 2.1 for gauges names):

- gauge 1: $\eta = 2.3407volt + 18.902$, R^2= 0.9714
- gauge 2: $\eta = 2.3407volt + 18.902$, R^2= 0.9714
- gauge 3: $\eta = 2.1746volt + 14.119$, R^2= 0.9939
- gauge 4: $\eta = 2.2434volt + 13.795$, R^2= 0.9959

2.2.2 PIV MEASUREMENT

Large Scale Particle Image Velocimetry (LS-PIV) was employed to measure the two-dimensional time dependent surface velocity fields $\mathbf{u}(x,y,t) = (u(x,y,t),v(x,y,t))$, where, according to the notations of Figure 2.1, we denote by x the landward oriented longitudinal axis of the channel with origin located in the basin at a distance of about 3 m from the channel inlet and by y the lateral coordinate; u and v are the x and y components of the velocity $\mathbf{u}$, respectively. PIV is a non

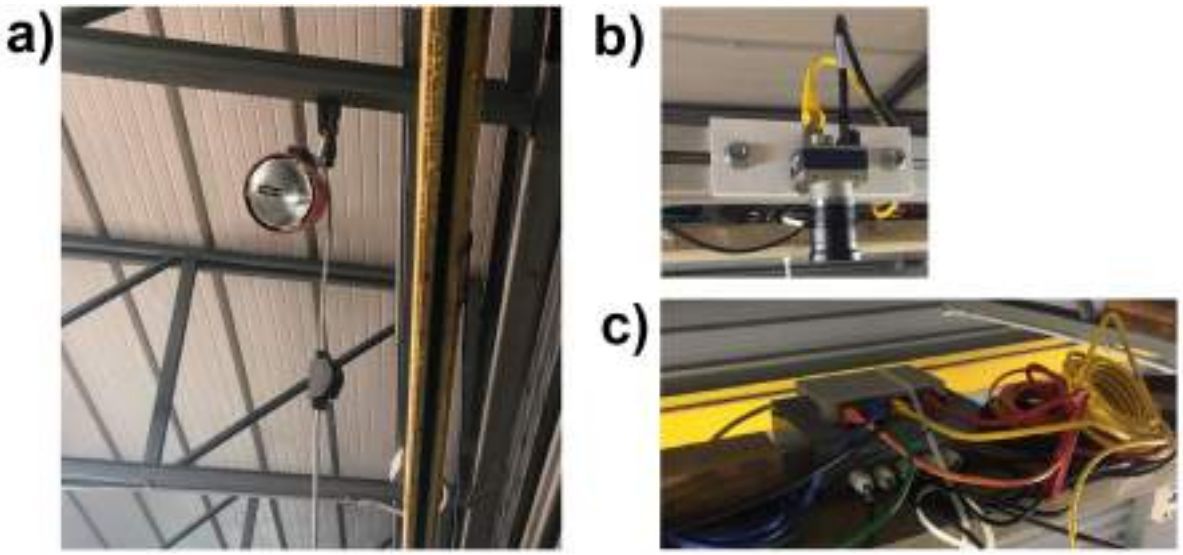

Figure 2.4: a) One of the eight halogen lamp; b) High-resolution GigaEthernet digital camera and c) High-data transfer switch and cabels.

intrusive optical method of flow visualization and it is used in a wide range of applications in order to obtain instantaneous velocity measurements, in particular when dealing with fluid velocity measurements (Raffel et al., 1998). By means of statistical methods, the local displacement for the images is determined assuming an homogeneous motion of the seeded tracers in the domain, between two consecutive time recordings. PIV technique allows for the calculation of the Eulerian velocity fields on the plane of measurement in case of 2D-PIV. It is worth noting that, in our application, the large dimension of the investigated area imposes specific equipment modifications with regards to the standard PIV technique. Indeed, the employment of a laser light is unfeasible owing to the large scale at hand. Lighting was thus produced using eight 500W white light halogen lamps (Figure 2.4a). The water surface was densely and uniformly seeded by polyethylene particles (940 kg m^{-3}, mean dimension 3 mm) used as PIV tracers.

LS-PIV acquisitions were recorded employing five high-resolution GigaEthernet digital camera (Teledyne Dalsa Genie Nano C1280 and C2450). Depending on the camera model, the resolutions varied between 2448×2048 pixels and 1280×1024 pixels. 6-mm lens have been mounted on the cameras. Cameras were fixed on rigid supports placed at an elevation of 4 m from the bottom of the channel, pointing downwards, as shown in Figure 2.1 and in detail in Figure 2.4b. In Figure 2.4c we report the high-data transfer switch that allows for a fast connection between

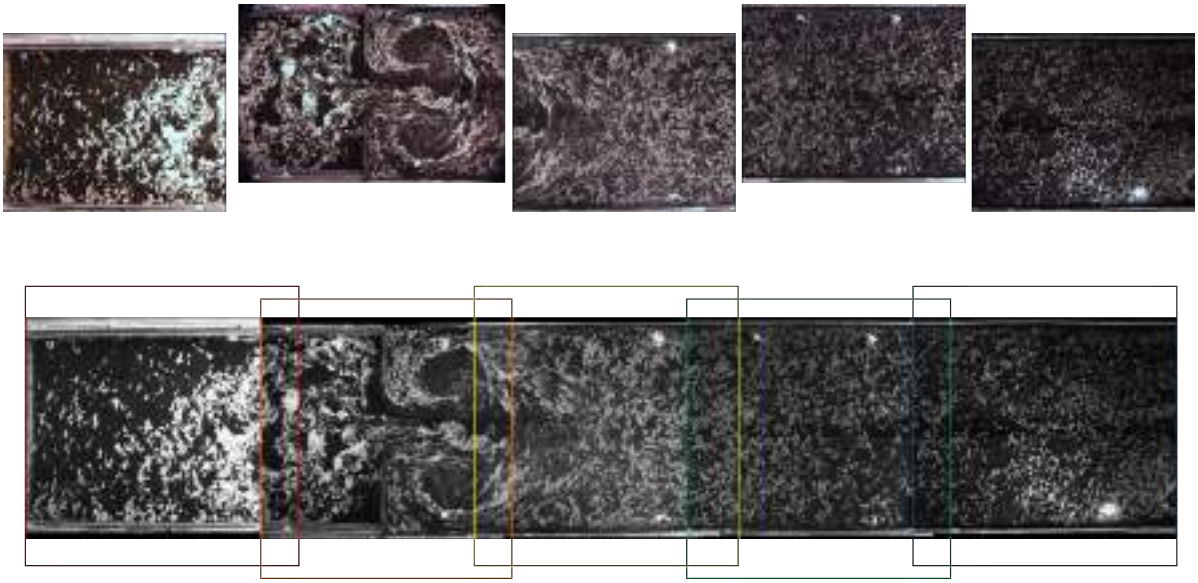

Figure 2.5: Five images acquired and panoramic image after merging process of a single time frame.

the cameras and the computer storage, in order to prevent data drops. Based on the camera arrangement, the Field of View (FoV) for the velocity measurements was such to cover a large area, including the inlet region, of about 13 × 2.2 m, extending from about the last 3 m of the basin to about the first 10 m of the channel for the entire width, with an image overlapping in the longitudinal direction of about 20%. The LS-PIV acquisition frame rate was set equal to 10 fps. The selected frame rate allowed for a detailed description of the time variation of the velocity fields: we obtained a number of velocity fields between 1000 and 1800 in a single tidal period depending on the imposed tidal wave. Note that a high-resolution set of experiments has been performed, in which we increased spatial and temporal resolution. This will be deeply exploited in Section 5.2. Depending on the set of experiments considered each camera recorded more than 5000 images (a single acquisition lasted about 5 tidal cycles). The images from the five digital cameras have been firstly binarized and then merged in order to obtain single panoramic images of the entire FoV for each temporal instant before PIV analysis. An example of the five recorded images and their merged panoramic view is shown in Figure 2.5. In particular, as described in Raffel et al. (1998), we followed the multi-frame/single exposure approach in which the temporal order of the particle position is preserved.

Finally, for the analysis of the images we employed the commercial software IDTproVision^{TM} PIV software. In particular, we took advantage of the *adaptive cell size* approach (Lourenco, 2000) that allows for the maximization of the cross-correlation between two consecutive images starting from an initial interrogation window. In our case, depending on the experimental parameter, the interrogation window varied from 24 × 24 pixels to 45 × 45 with a maximum overlap of 50%, ending up with about 15 thousand velocity vectors. Based on our PIV analysis settings and, in particular, the size of the interrogation window and cross-correlation template, the final spatial resolution was about one vector every 5.8 cm along the x-coordinate and 3.5 cm on the y-coordinate. This experimental approach, based on the free surface velocity measurement, is often used in many experimental works with primary focus on quasi-2D vortical structures (see Jirka (2001); Nikora et al. (2007); Nicolau del Roure et al. (2009) among others).

CHAPTER 3

THEORETICAL BACKGROUND

In this chapter we briefly introduce the background theory on which we based our flow field analysis. In particular, we started from an Eulerian approach to pass through a Lagrangian one. Just to recall, approaching the flow analysis in an Eulerian manner consists in considering a control volume of fluid and observe how the flow characteristics change within the volume, whereas the Lagrangian method focus on changes of a particular fluid particle that must be followed during the entire time span of study. Moreover, in the latter context, it is also possible to distinguish between homogeneous and non-homogeneous quantities through which a distinction between an average behaviour and a local analysis of the process can be provided.

3.1 EULERIAN APPROACH

In fluid mechanics, a fluid element may experience four type of motion or deformation such as translation, rotation, linear strain and shear strain. They may also occur simultaneously, further complicating the analysis at hand, forcing us to study the dynamics in terms of *rates*. The deformation rates are then expressed in terms of velocities and derivatives of velocity. The rate of translation vector, in particular, is described by the velocity vector itself. In a two dimensional flow field, the vertical component is neglected thus the velocity can be written as

$\mathbf{u}(x,y,t) = (u(x,y,t), v(x,y,t))$. The rate of rotation, i.e. the vorticity, is defined as the curl of the velocity that in 2D is

$$\omega_z = \frac{\partial v}{\partial x} - \frac{\partial u}{\partial y} \tag{3.1}$$

and it represents the measure of rotation of a fluid particle. Nonzero vorticity determines a rotation of the fluid particles within the domain: the flow in that region is called *rotational*; otherwise the fluid particles are not rotating and the flow is described as *irrotational*. Note that a zero vorticity flow does not imply straight streamlines: circular streamlines may occur also in irrotational flows. In order to highlight regions characterized by high concentrations of vorticity, we performed an eigenvalue analysis on the Jacobian of the velocity

$$J_{ij} = \frac{\partial u_i}{\partial x_j}. \tag{3.2}$$

The aim is to describe the flow topology, finding the critical points from which infer vortex estimators such as the swirling strength λ_{ci} (Zhou et al., 1999; Adrian et al., 2000) and Okubo-Weiss parameter λ_0 (Okubo, 1970; Weiss, 1991).

In non linear dynamical analysis, the study of the eigenvalues of the characteristic equation (Chong et al., 1990)

$$det(\mathbf{J} - \lambda \mathbf{I}) = 0 \tag{3.3}$$

allows for recognition of flow features. The characteristic equation could be also written in terms of the trace and determinant of $\mathbf{J}$, i.e.

$$\lambda^2 - \tau\lambda + \Delta = 0 \qquad with \qquad \tau = tr(\mathbf{J}) \qquad and \qquad \Delta = det(\mathbf{J}) \tag{3.4}$$

that has two solutions

$$\lambda_1 = \frac{\tau + \sqrt{\tau^2 - 4\Delta}}{2} \qquad and \qquad \lambda_2 = \frac{\tau - \sqrt{\tau^2 - 4\Delta}}{2} \tag{3.5}$$

in which τ and Δ allow for the representation of the phase portrait as seen in Figari and Altosole (2007) from which Figure 3.1 belongs. Real and distinct eigenvalues correspond to linear independent eigenvectors, along which all the trajectories asymptotically approach, with the direction of time chosen appropriately. In particular, both positive (negative) eigenvalues determine stable

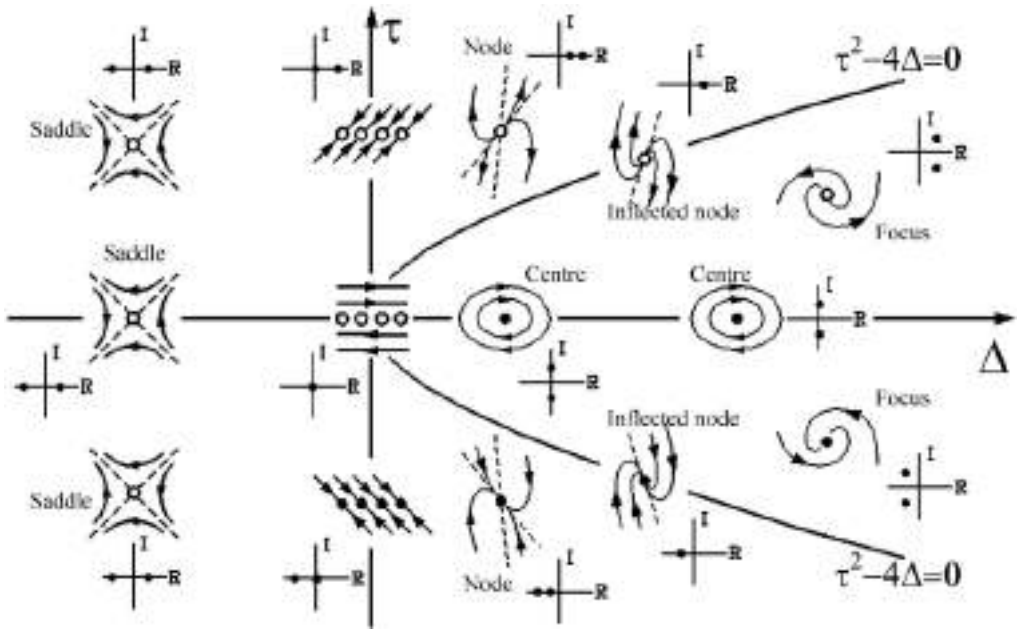

Figure 3.1: Phase Portrait

(unstable) points, whereas eigenvalues with opposite signs highlight saddles. Complex eigenvalues indicate stable (unstable) elliptical flow regions. Indeed, we denote the swirling strength as the complex part of the complex eigenvalues and it represents zones characterized by high rotational velocities.

Another vortex estimator could be the Okubo-Weiss parameter (Okubo, 1970; Weiss, 1991). For steady or slowly time dependent flows, the Okubo-Weiss criterion makes use of the eigenvalues of the local velocity gradient tensor **D**

$$\nabla \boldsymbol{v} = \begin{vmatrix} \frac{\partial u}{\partial x} & \frac{\partial u}{\partial y} \\ \frac{\partial v}{\partial x} & \frac{\partial v}{\partial y} \end{vmatrix} \tag{3.6}$$

which can be written as $\nabla \boldsymbol{v}^2 = \lambda_0 \mathbf{I}$, where the Okubo-Weiss parameter $\lambda_0 = -\det(\nabla \boldsymbol{v})$ is the product of the eigenvalues of $\nabla \boldsymbol{v}$. However, it is better to write it in the form suggested by Weiss (1991) as $\lambda_0 = \frac{1}{4}(S^2 - \omega^2)$ where $S^2 = S_n^2 + S_s^2$ is the total square strain, sum of the normal (S_n) and shear (S_s) components,

$$S_n = \frac{\partial u}{\partial x} - \frac{\partial v}{\partial y} \qquad S_s = \frac{\partial v}{\partial x} + \frac{\partial u}{\partial y} \tag{3.7}$$

and ω^2 the square vorticity, as defined in equation 3.1. The sign of λ_0 discriminates between locally hyperbolic flow regions ($\lambda_0 > 0$ strain dominated) and locally elliptical flow regions

($\lambda_0 < 0$ rotation dominated). The latter are signature of coherent vortices. Note that both the aforementioned estimates are not objective, that means not invariant in respect with rotations and this suggests further developments towards a vortex identification using a pure Lagrangian approach. Examples of use of this kind of criteria employed for the identification of vortex structures can be found in Zhou et al. (1999); Adrian et al. (2000); Stocchino et al. (2011), among others. In particular, Zhou et al. (1999) and Adrian et al. (2000) took advantage of the definition of the local swirling strength for the identification of the vortices in a mean turbulent field characterized by a low-Reynolds-number flow, whereas Stocchino et al. (2011) evaluated the Okubo-Weiss parameter in a straight compound channel under quasi-uniform flow conditions.

3.2 HOMOGENEOUS LAGRANGIAN APPROACH

3.2.1 SINGLE PARTICLE STATISTIC

The most natural framework for analyzing mixing processes is the Lagrangian (or material) one, which studies the evolution of material particles during the flow motion. Lagrangian statistics thus average on particle positions, in terms of single or pairs or groups of particles (absolute and relative statistics respectively). A description of these statistics is briefly provided. Given an Eulerian velocity field it is possible to compute trajectories of material particles by integrating the equation:

$$\frac{d\mathbf{x}(t)}{dt} = \mathbf{u}(\mathbf{x}, t) \tag{3.8}$$

where $\mathbf{x}$(t) is the position at time t of the given particle and $\mathbf{u}(\mathbf{x}, t)$ is the Eulerian velocity at point $\mathbf{x}$ and time t. Once the particle trajectories are known, the absolute dispersion tensor, $\mathbf{A}^2(t, t_0)$, can be found as (Provenzale, 1999):

$$A_{ij}^2(t, t_0) = \frac{1}{M} \sum_{m=1}^{M} \left\{ \left[x_i^m(t) - x_i^m(t_0) \right] \left[x_j^m(t) - x_j^m(t_0) \right] \right\} \tag{3.9}$$

where M is the number of particles and $\mathbf{x}^m(t)$ is the position of the m-th particle at time t and $\mathbf{x}^m(t_0)$ its initial position. The mean square displacement is given by the trace of $\mathbf{A}^2(t)$, and it is defined as the total absolute dispersion, which reads:

$$a^2(t) = Tr(\mathbf{A^2}) \tag{3.10}$$

The time derivative of $a^2(t)$ provides the estimate of the total absolute diffusivity coefficient $K(t)$ (Taylor, 1921; Provenzale, 1999; LaCasce, 2008).

Classical dispersion regimes are identified based on the time dependence of the total absolute dispersion following the theory of Taylor (1921), found to be valid in several geophysical context (LaCasce, 2008). The time dependence of the diffusivity coefficients enables the identification of different dispersion regimes (Provenzale, 1999; Boffetta et al., 2001): in a wide variety of applications, the absolute dispersion obeys power laws of the type $\mathbf{A}^2(t,t_0) \simeq t^\alpha$ and, therefore, the absolute diffusivity can be described as $K(t) \simeq t^{\alpha-1}$. The fundamental results obtained by Taylor (1921) in the case of homogeneous turbulence show that, for short times after particles' deployment, an exponent $\alpha = 2$ can be expected, describing the so-called *ballistic regime*. For times longer than an integral time scale T_L, defined as the decorrelation time, the exponent should be $\alpha = 1$, the so-called diffusive or Brownian regime.

The decorrelation time, the so-called Lagrangian integral scale T_{L_i}, is defined as the time needed by a particle to loose memory of its initial position. In particular, it separates the quadratic and the linear time dependence of the absolute dispersion. It is defined as the time integral of the Lagrangian autocorrelation function of the i-th Lagrangian velocity component u_{L_i} as:

$$T_{L_i} = \int_0^{+\infty} \mathscr{R}_{ii} d\tau \tag{3.11}$$

where

$$\mathscr{R}_{ii}(\tau) = \frac{1}{M} \sum_M \frac{\rho_{L_{ii}}(\tau)}{\sqrt{\rho_{L_{ii}}(0)\rho_{L_{ii}}(0)}} \qquad and \qquad \rho_{L_{ii}}(\tau) = \langle u_{L_i}(t) u_{L_i}(t+\tau) \rangle \tag{3.12}$$

in which the brackets indicate an average over the entire duration of each trajectory and u_{L_i} is the i-th component of the Lagrangian velocity. The Lagrangian integral scale is then computed as

$$T_L = \frac{1}{2}\left(T_{L_x} + T_{L_y}\right) \tag{3.13}$$

A detail review can be found on LaCasce (2008). Elhmaïdi et al. (1993) discussed the single particle dispersion of neutrally buoyant particles in two-dimensional turbulent flows finding that coherent structures and circulation cells may affects the single-particle dispersion properties.

3.2.2 MULTIPLE PARTICLE STATISTICS

Being interested in discussing the interplay among the particle trajectories and the different scales of the flow, we apply tools commonly reported as multiple particle statistics (see LaCasce (2008) for a review and application to geophysical contexts). Differently from the single particle statistics, here we follow the separation of couple of particles in time, computing the relative dispersion. The relative dispersion matrix $\boldsymbol{R}^2(r_0,t)$ is defined as the mean-square distance at time t between a pair of particles that at time t_0 had a distance equal to r_0:

$$R^2_{ij}(r_0,t) = \frac{1}{M-1}\sum_{m=1}^{M-1}\left\{\left[x_i^m(t)-x_i^{m+1}(t)\right]\left[x_j^m(t)-x_j^{m+1}(t)\right]\right\} \tag{3.14}$$

here $M-1$ is the number of particle pairs. As for the total absolute dispersion a^2, the total relative dispersion $r^2(t)$ is simply the trace of the relative dispersion matrix $\boldsymbol{R}^2(r_0,t)$ and the total relative diffusivity $D(t)$ is its time derivative.

Studies of the multiple statics can be found in Boffetta et al. (2001); Biferale et al. (2005); Bec et al. (2010).

Together with the relative dispersion, we employ another Lagrangian measure commonly used in dispersion studies, namely the Finite Scale Lyapunov Exponents Λ (FSLE). FSLE consists in averaging the times required to a pair to separate from an initial distance to a final one (Artale et al. (1997); LaCasce (2008); Cencini and Vulpiani (2013)). FSLEs provide a measure of the dispersion as a function of the spatial resolution (Boffetta et al., 2001). This Lagrangian measure allows for the identification of the most dynamic regions, i.e. the places of maximum and minimum expansion of the fluid domain. The aim is to evaluate the time needed for a pair of particles to reach a defined final separation. Thus, in order to calculate the FSLE it is necessary to first choose a set of distances that are recursively increased as:

$$r_n = \delta r_{n-1} = \delta^n r_0, \tag{3.15}$$

where n is the chosen number of separation and δ is an arbitrary constant larger than unity, and then calculate the times required (known as "exit time" T_n) for each pair displacement to grow to the successive r_n. At each distance the maximum FSLE is computed as:

$$\Lambda(r_n) = \frac{1}{\langle T_n\rangle}\log(\delta), \tag{3.16}$$

where the brackets indicate an ensemble average over the particle pairs that effectively reach the r_n distance. Care must be taken in the choice of the multiplier δ in order to correctly capture the regimes of the flow at hand (Haza et al., 2008). In our experiments, we set δ = 1.2 as seen in Enrile et al. (2019).

Both relative dispersion and FSLE have been extensively used in oceanographic and costal studies leading to a better comprehension of the physical processes at the different separation scales (Artale et al., 1997; Orre et al., 2006; LaCasce, 2008; Haza et al., 2008; Enrile et al., 2018b, 2019).

The success of the use of the two measures in geophysical applications relies on classical studies on 2D and atmospheric turbulence (Kraichnan, 1966; Lin, 1972; Er-El and Peskin, 1981; Bennett, 1984; Babiano et al., 1990). The main results were the existence of two distinct dynamical mechanisms leading to two dispersion regimes, namely *local dispersion* and *non-local dispersion* and the link between the scaling law of these regimes with the energy cascade (inverse energy cascade and direct enstrophy cascade). Scaling arguments to describe the different dispersion and energy regimes can be summarized searching for laws of the kind:

$$D \propto r^{(\alpha+1)/2}. \tag{3.17}$$

The link with the energy cascades is the value of the exponent α, having assumed the turbulent energy spectrum as a function of the wave numbers in the form of $E(k) \propto k^{-\alpha}$.

Relative dispersion in *local dynamics* is characterized by the effect of local straining, which is not efficient in producing large separation, and the dispersion of pairs is dominated by eddies of the same scale of their separation. This regime is described by values $1 < \alpha < 3$ and, in particular, for $\alpha = 5/3$ the famous Richardson-Obukhov law is recovered with $D \propto r^{4/3}$, that corresponds to the energy cascade $E(k) \propto k^{-5/3}$. On the contrary, *non-local dynamics* is characterized by the effect of vortices with typical scale much larger than the separation. This regime is described by the Kraichnan-Lin law $D \propto r^2$, or more generally for $\alpha > 3$. In this case, the expected energy spectrum corresponds to an enstrophy cascade $E(k) \propto k^{-3}$.

Note that where the relative dispersion shows a power law dependence, the FSLEs exhibit a power law dependence on the separation as $\Lambda \propto r^{-2/\beta}$. The exponent β is linked to the time

growth of r^2 with time (LaCasce, 2008).

3.3 Inhomogeneous Lagrangian approach

In environmental mixing processes, spatial inhomogeneities may occur owed to obstacles in the flow field and changes in the geometry. The spreading of material particles from their initial position may be enhanced or weaken according to the local velocity at which they are subjected. The great variability in space and time of the flow led the homogeneous quantities previously introduced (single and multiple statistics) useful tools in the definition of the overall process but is still lacking of information, since they result from a spatial average of regions characterized by different dynamical behaviours.

It worth noting that despite turbulent character of the flow, it is still possible to recognize large-scale coherent structures (Shadden et al., 2005) that help for a deeper understanding of the flow dynamics, even in the spatial resolution. FTLE-LCS approach, indeed, claims that coherent structures in a flow represent surfaces of large separations, i.e. they act as transport barriers, and allow for distinguish flow regions with different dynamical behaviours. Moreover, the time dependence of the LCS is able to describe the transport mechanism among different regions of the domain in time.

Here we introduce the method of extracting Lagrangian Coherent Structures (LCS) by means of the Finite Time Lyapunov Exponents (FTLE). LCS was first developed by Haller and Yuan (2000), and then further studied by Shadden et al. (2005); Lekien et al. (2005); Haller and Beron-Vera (2012), among many others. The Lagrangian approach, which employs particle trajectories that necessarily retain the time-dependence in the velocity field, is more effective in identifying persistent coherent structures than the Eulerian methods. Moreover, LCS has the advantage that can be directly used on non-periodic flows, and to flows that are defined by discrete data sets over a finite time interval.

3.3.1 Finite Time Lyapunov Exponents

Applying the well-known principles of the continuum mechanics, we will define the Finite Lyapunov Exponents. In order to describe the position of particles ξ of a fluid body $\mathscr{B}$, we define

a one-to-one correspondence between the particles and the coordinates of a reference system. The Lagrangian coordinates then read $\boldsymbol{\xi} = \left(\xi^1, \xi^2, \xi^3\right)$ and defines a label for fluid particles as a material coordinate system. At this point, it is possible to define a continuous and differentiable transformation $\boldsymbol{\Phi}$, called *flow map*, that allows a link between the Lagrangian and the Eulerian coordinate system:

$$x = \boldsymbol{\Phi}(t, t_0, \boldsymbol{\xi}). \tag{3.18}$$

This transformation can be inverted in a point neighborhood, provided that Jacobian exists and does not vanish (Aris, 1962). Note that the study of fluid flow cannot be fulfilled disregarding the velocity fields. Indeed, the particles trajectories are solutions of equation (3.8) with initial conditions $\mathbf{x}(t_0, \boldsymbol{\xi}) = \boldsymbol{\xi}$. With the aim to evaluate the distance that two initial close particles $\boldsymbol{\xi}_0$ and $\boldsymbol{\xi}_0 + \epsilon$ may experience on a finite time interval $T = (t_0, t_1)$, we can apply a linearization (Allshouse and Peacock, 2015) such as:

$$\delta\mathbf{x} = \boldsymbol{\Phi}(t_1, t_0, \boldsymbol{\xi}_0) - \boldsymbol{\Phi}(t_1, t_0, \boldsymbol{\xi}_0) + \epsilon \approx \nabla\boldsymbol{\Phi}(t_1, t_0, \boldsymbol{\xi}_0)\epsilon \tag{3.19}$$

where ϵ represents an infinitesimal perturbation and $\nabla\boldsymbol{\Phi}(t_1, t_0, \boldsymbol{\xi}_0)$ is the tensor flow map gradient (Figure 3.2a)) defined as

$$\nabla\Phi^i_j = \partial x_i / \partial \xi_j. \tag{3.20}$$

Note that we impose that an infinitesimal material element dx must not split along its evolution and coalescence of two material elements does not occur: this is the physical interpretation of the condition on the Jacobian of equation (3.18). Moreover, the deformation must preserve orientation, that is three right-handed material elements dx, dy and dz satisfying $dx \wedge dy \cdot dz > 0$ are transformed into three material elements satisfying

$$dx(t) \wedge dy(t) \cdot dz(t) = (\nabla\boldsymbol{\Phi} dx) \wedge (\nabla\boldsymbol{\Phi} dy) \cdot (\nabla\boldsymbol{\Phi} dz) = det(\nabla\boldsymbol{\Phi}) dx \wedge dy \cdot dz > 0. \tag{3.21}$$

This second restriction implies that the Jacobian of equation 3.18 must satisfy:

$$J = det(\nabla\boldsymbol{\Phi}) > 0 \tag{3.22}$$

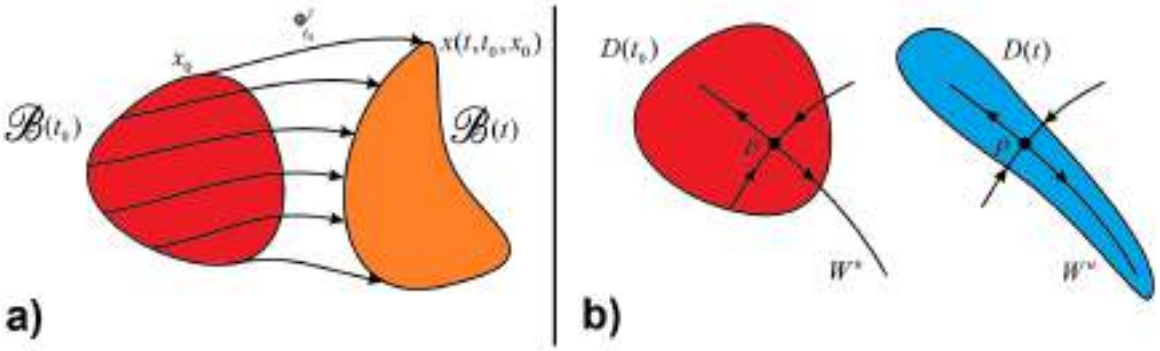

Figure 3.2: a) The deformation of a tracer blob under the flow map $\mathbf{\Phi}_{t_0}^{t}$. b) Outward fingering-type instability of a tracer pattern in a steady flow, caused by as saddle point p located inside the initial tracer distribution.

The magnitude of the final distance can be evaluated as (Shadden et al., 2005):

$$|\delta\boldsymbol{x}(t_1)| = \sqrt{\delta\boldsymbol{x}(t_1)\cdot\delta\boldsymbol{x}(t_1)} = \sqrt{[\nabla\Phi\delta\boldsymbol{x}(t_0)]\cdot[\nabla\Phi\delta\boldsymbol{x}(t_0)]} = \\ = \sqrt{\delta\boldsymbol{x}(t_0)\cdot[\boldsymbol{C}\delta\boldsymbol{x}(t_0)]} = \sqrt{\epsilon\cdot(\boldsymbol{C}\epsilon)} \tag{3.23}$$

where $\boldsymbol{C}$ is the Cauchy-Green tensor evaluated as

$$\boldsymbol{C} = (\nabla\mathbf{\Phi})^T\nabla\mathbf{\Phi} \tag{3.24}$$

where $(\bullet)^T$ denotes the transpose. It is possible to prove that matrix $\boldsymbol{C}$ is positive definite and symmetric. Since we analyse 2D velocity fields, $\boldsymbol{C}$ has two eigenvectors e_1 and e_2 associated with two eigenvalues $0 < \lambda_1 \leq \lambda_2$, respectively. This means that two main directions can be recognized, tangent to the eigenvectors associated with the maximum and minimum eigenvalues and called unstable and stable directions respectively, and in particular the magnitude of a concentration gradient will decay in time along the unstable direction (Thiffeault and Boozer, 2001). In particular, let's consider for example a saddle point p within an initial tracer distribution $\mathscr{B}(t_0)$, with its unstable manifold W^u intersecting the boundary of $\mathscr{B}(t_0)$ at a nonzero angle. The material will be transported exponentially fast by the flow map along this unstable manifold, leading to a fingering-type instability (Olascoaga and Haller, 2012). The unstable manifold is thus a *stretching* line, see Figure 3.2b). When $\delta\boldsymbol{x}(t_0)$ is aligned with the eigenvector associated to the maximum eigenvalue of $\boldsymbol{C}$, the maximum stretching occurs:

$$\max|\delta\boldsymbol{x}(t_1)| = e^{\sigma_{t_0}^{t_1}|T|}|\bar{e}| \tag{3.25}$$

where

$$\sigma_{t_0}^{t_1} = \frac{1}{|T|} \log \sqrt{\lambda_2} = \frac{1}{2|T|} \log \lambda_2 \tag{3.26}$$

represents the (maximum) Finite-Time Lyapunov Exponent (FTLE) calculated on a finite integration time T. Note that a coordinate transformation does not produce any changes in FTLE calculation: for this reason FTLE are considered *objective* quantities. Computing σ in forward time ($t \gg t_0$), repelling manifold at t_0 are recognized to be the local maxima (i.e. *ridges*) of the $\sigma_{t_0}^{t_1}$ and, similarly, the attracting ones correspond to ridges in the $\sigma_{t_0}^{t_1}$, calculated in backward time ($t \ll t_0$).

3.3.2 Lagrangian Coherent Structures

LCSs are usually associated with ridges and trenches of FTLE (Shadden et al., 2005; Haller and Beron-Vera, 2012). They depict the most repelling, attracting, and shearing material surfaces with the aim to describe and quantify the material transport, and forecast large-scale flow features and mixing processes (Haller, 2015). Following the definition of Mathur et al. (2007), a ridge in FTLE field, that behaves as an attractor, is the solution of

$$\frac{d\mathbf{x}_0}{ds} = \nabla \sigma_{t_0}^{t_1}(\mathbf{x}_0) \tag{3.27}$$

with s the arclength along the gradient lines. As pointed out by Shadden et al. (2005), LCS ridges are FTLE's gradient lines transversal to the minimum curvature direction, across which the flux is usually negligible (even if non zero) and hence they act as transport barriers. Haller (2011) improved the above definition stating that, in order to be recognized as a LCS, two key properties must be respected: FTLE should be a material surface (as already said by Shadden et al. (2005)) and should exhibit locally the strongest attraction, repulsion, and shearing in the flow. This latter aspect is linked with the *hyperbolicity criterion*: it enables to observe LCS as cores of Lagrangian patterns. In particular, finding the local maxima in FTLE does not identify LCS, indeed it has been found out by Lekien et al. (2005) and Tang et al. (2010) that FTLE in real-data sets could also nor attract or repel nearby trajectories. Thus, four condition must hold in order for an FTLE to be a LCS ridges:

- λ_2 of $\sigma_{t_0}^{t_1}$ must be larger that one with one-multiplicity, $\lambda_1 \neq \lambda_2 > 1$;
- FTLE ridge has to be normal to the eigenvector of λ_2, $\mathbf{e}_2(\mathbf{x}_0)$, field;
- the gradient of λ_2 in directions parallel to $\mathbf{e}_2(\mathbf{x}_0)$ must be small $\langle \nabla\lambda_2(\mathbf{x}_0, t_0, T), \mathbf{e}_2(\mathbf{x}_0)\rangle = 0$;
- FTLE must be steep, i.e. the Hessian of the Cauchy-Green tensor evaluated on the strongest strain eigenvector field is positive, $\nabla^2\mathbf{C}^{-1}(\mathbf{x}_0) > 0$.